# ROOTS DISTRIBUTION OF RANDOM SEQUENCES: NEW METHOD OF SUPERWEAK SIGNALS DETECTION

R.R. NIGMATULLIN[1], D. BALEANU[2,3], O. TINTAREANU-MIRCEA[3], A. TCHELDERIAN[2]

[1] Kazan National Research Technical University named after A.N. Tupolev, Radioelectronics and Informative Measurements Technics Department, Kazan, Tartastan, Russia
*E-mail*: renigmat@gmail.com
[2] Department of Computer Science and Mathematics, Lebanese American University, Beirut, Lebanon
*E-mails*: dumitru.baleanu@lau.edu.lb; ayk.tchelderian@lau.edu
[3] Institute of Space Science – INFLPR subsidiary, Magurele-Bucharest, Romania
*E-mail*: ovidiu@spacescience.ro

*Received November 25, 2025*

*Abstract.* In this paper, the authors propose a novel method for analyzing random sequences that exhibit or lack a clearly expressed trend. The idea is based on calculating the roots defined by the intersection of the horizontal line with the given sequence. The final Roots Distribution (RD) curve formally resembles conventional statistical distributions or histograms; however, it has one key difference: the number of roots is obtained using a distinct algorithm compared to the conventional method for calculating histograms. The Generalized Pareto Distribution (GPD), incorporating three power-law exponents, can be used to fit the obtained branches of the RD. It is possible for complex-conjugated exponents to appear during this fitting procedure. When this method is applied to sequences with a trend, the RD transforms into a specific spectrum that features many peaks. This proposed methodology is applied to the detection and quantitative description of extremely weak gravitational wave (GW) signals, such as those emitted by Extreme Mass Ratio Inspirals (EMRIs). This RD enables the quantitative description of the GW signal and the noise that completely obscures it. Furthermore, one can subtract the expected GW (obtained a priori or analytically from the detected noise) and transform it to the RD of the second type as a specific fingerprint for its certain detection.

*Key words*: Roots distribution spectra; Gravitational waves with noise and their detection; The generalized Pareto distribution.

DOI: https://doi.org/10.59277/RomJPhys.2026.71.104

## 1. INTRODUCTION AND PROBLEM FORMULATION

EMRIs are a class of binary systems consisting of a low-mass compact object (CO), such as a neutron star or stellar black hole, spiraling around a supermassive black hole (SMBH). The term “extreme mass ratio” reflects the extreme ratio between the two masses, typically between $10^{-4}$ and $10^{-7}$. The CO orbit is determined by the geodesics of the SMBH’s space-time and evolves slowly over time, through loss of energy and angular momentum and the emission of GWs. This slow evolution allows hundreds of thousands to millions of cycles to be performed in the frequency band of GW space observatories, making EMRIs excellent sources to test the general relativity (GR) in regimes of intense gravitational fields [1, 2].

The frequency of GW emitted by EMRI is in the range of 0.1 mHz and 0.1 Hz, which makes them detectable only by space observatories such as LISA (Laser Interferometer Space Antenna), ground-based detectors such as LIGO or Virgo having arms too small to be sensitive to such low frequencies. LISA will be able to observe EMRI from cosmological distances [3], which transforms EMRIs into cosmological probes and unique tools for understanding the distribution of SMBH in the Universe [4, 5].

By precise analysis of the GW emitted by EMRI, it will be possible to determine the source parameters such as the mass and spin of the SMBH, the distribution of dark matter around it, the orbital characteristics of the CO, the distance to the source and even its position in the sky. EMRIs cam become laboratories for testing the "no-hair" theorem of black holes, one of the fundamental predictions of GR [6]. Also, any deviation from the expected signature of a Kerr space-time may be an indication of new physics, such as modified gravity or the existence of exotic COs [7].

EMRIs can also help constrain cosmological parameters, such as the Hubble constant or the nature of dark energy, by correlating gravitational signals with electromagnetic sources or by using them as "standard sirens" [8]. In addition, the EMRI distribution can be used to better understand the history of galactic mergers and galaxy formation in the early Universe [9].

Despite all this promise, the EMRI signal is extremely weak, often deeply buried in the background noise of the instrument and in the noise produced by other unresolved gravitational sources (such as galactic binaries) [10, 11]. Detecting this signal requires exceptional sensitivity and extremely sophisticated data analysis methods. The matched filtering technique, successfully used in LIGO, is difficult to use here because of the huge number of parameters describing the EMRI signal: mass, spin, inclination, eccentricity, initial phases, position on the sky, etc. [12]. Instead, Bayesian methods such as MCMC (Markov Chain Monte Carlo), Nested Sampling or Hamiltonian Monte Carlo [13, 14] can be used. These methods can efficiently navigate the large parameter space, but are computationally intensive. To speed up the detection and estimation of parameters, hybrid methods based on deep learning are explored [15, 16]. Convolutional neural networks are used for signal classification, while autoencoders and recurrent networks are applied for noise removal or filling in missing portions of the signal [17].

Noise characterization is an essential step in the EMRI detection process. The noise in LISA is composed of several components: instrumental noise (laser noise, shot noise, optical noise, residual acceleration noise, thermal noise), galactic noise (the unresolved background produced by millions of compact galactic binaries) and confusion noise (overlapping sources). Reducing this noise requires both source separation methods (Independent Component Analysis, Principal Component Analysis) and adaptive methods that can learn the noise signature and eliminate it [18, 19]. Furthermore, generative adversarial networks algorithms are trained to generate artificial noise and improve the robustness of detection models [20].

EMRI signal modeling is itself a vast research area. The most accurate models include gravitational self-interaction (self-force) effects, obtained by perturbative methods in GR [21]. The kludge-type models approximate the signal using modified Newtonian orbits or relativistic orbits on a Kerr space-time background and are computationally faster. Recently, surrogate models, which use interpolation between dense numerical simulations or neural networks trained on simulated data, allow the rapid generation of realistic waveforms for EMRI [22].

The importance of EMRI is also reflected in the international effort to prepare algorithms and technologies for their detection. LISA Data Challenge were launched to simulate the real data that will be collected by LISA and to test the ability of the scientific community to extract EMRI signals [23]. These challenges led to the development of sophisticated software tools, capable of separating EMRI from other sources and noise, estimating source parameters and quantifying associated uncertainties [24].

Inevitably, the analysis of EMRI data will require a massive computational infrastructure. Distributed processing networks, parallel processing on GPUs, algorithmic optimizations and probably integration into cloud analysis platforms [25] will be required. The gravitational community is also exploring the integration of EMRI sources into global LISA data analysis models, which would simultaneously treat all sources present in the observed signal, in a holistic approach [26].

Summarizing, EMRIs offer a unique window into a yet unexplored regime of the Universe such as the space-time in the vicinity of SMBHs. They make valuable contributions to fundamental physics, astrophysics and cosmology, but also impose major challenges for observational technology, numerical modelling and data analysis. Their detection will only be possible through concerted efforts at the intersection of physics, applied mathematics, computer science and engineering. In preparation for the LISA mission, the continued development of noise reduction methods, signal modelling and Bayesian analysis is crucial to harness the unprecedented scientific potential of these extraordinary GW sources.

In the present paper, we investigated the fundamental problem of whether the Roots Distribution Spectroscopy (RDS) can be used to detect a superweak EMRI GW signal completely hidden within noise. From the author's point of view, this is a completely new instrument for the elimination of residual noise of any nature. Undoubtedly, it will occupy a significant place in the analysis and processing of superweak signals. Section 2 describes the analyzed data, which will be processed in a subsequent section. Section 3 details the data treatment procedure, emphasizing the most attractive features of the proposed method. Finally, results and discussion are presented in Section 4.

## 2. DESCRIPTION OF DATA

In this paper, we analyzed three gravitational EMRI waveforms (WF) (see Fig. 1), specifically varying the initial eccentricity $e_0$ and inclination $\iota_0$ of the CO orbit relative to the SMBH spin. The remaining intrinsic and extrinsic parameters were set to the following values: $M = 10^6\, M_\odot$ (central SMBH mass in terms of solar masses), $m = 10\, M_\odot$ (CO mass in terms of solar masses), $a = 0.2$ $\phi_\varphi = 0.2$, $p_0 = 9$ (initial semilatus-rectum of the CO orbit), $\phi_\theta = 1.2$, $\phi_r = 0.8$ (initial phases), $q_S = 0.2$, $\varphi_S = 0.2$, $q_K = 0.8$, $\varphi_K = 0.8$ (polar/azimuthal spin/viewing angles); $D = 1.0$ Gpc (distance), d$t = 15.0$ s (sampling rate in seconds) $T = 12$ hours (observation time).

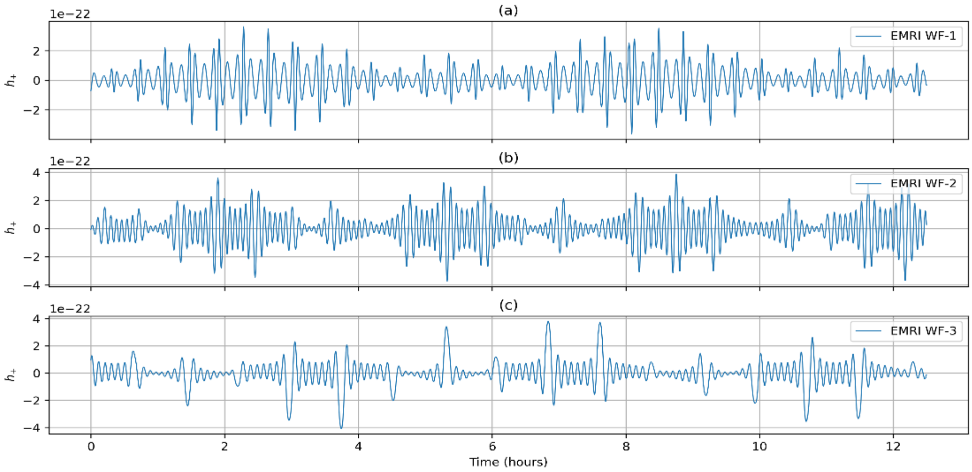


Fig. 1 – The three EMRI WF that were analyzed. The varied parameters are: $e_0 = 0.4$, $\iota_0 = 0.9$ for WF-1 (a), $e_0 = 0.4$, $\iota_0 = 2.1$ for WF-2 (b), and $e_0 = 0.7$, $\iota_0 = 2.1$ WF-3 (c).

In GR, GWs are composed of a linear combination of two transverse polarization modes, commonly referred to as plus (+) and cross (×) tensor modes, therefore the WF is usually decomposed as $h = h_+ + ih_\times$. Although the FEW package provides both $h_+$ and $h_\times$, we utilized only the $h_\times$ data for this work.

The EMRI waveforms were then combined with white Gaussian noise of different amplitudes. The SNR of the noisy signal varies from hundredths to tens and was calculated simply as the ratio of signal power to noise power. This straightforward approach was adopted because, in this initial step, the GW signal was not passed through a simulated detector.

Figure 2 displays one of the three EMRI waveforms (WFs) immersed in Gaussian background noise. Four corresponding SNR levels are shown, decreasing from top to bottom: 14.5, 1.6, 0.4, and 0.06.

EMRI GWs were simulated using the 5PN AAK algorithm from the Fast EMRI Waveform (FEW) package, suitable for generic Kerr inspirals.

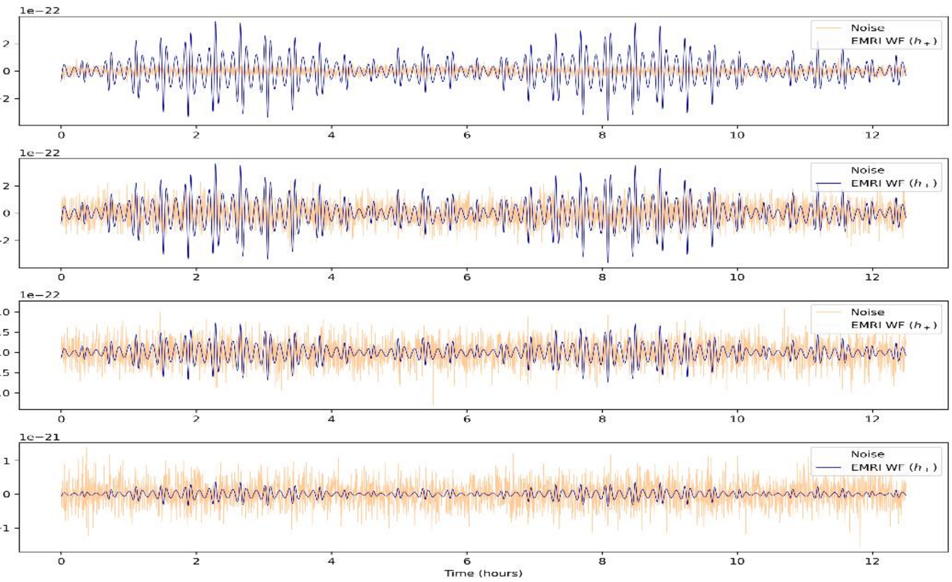


Fig. 2 – The first (Subplot (a) of Fig. 2) of the three EMRI waveforms (WF-1) immersed in four different levels of white Gaussian noise.

## 3. DESCRIPTION OF DATA TREATMENT PROCEDURE

### 3.1. ANALYSIS OF TRENDLESS SEQUENCES

The original data processing procedure for trendless sequences is based on a root-counting method derived from the intersections with a horizontal line. This horizontal line mimics a pseudo-quantum spectrum, ranging from the minimal to the maximal values of the given trendless sequence. If the given trendless sequence occupies the interval (–$A$, $B$) then one might expect that maximal number of the roots will be concentrated near abscissa axes OX. This RD envelope can serve as a quantitative measure, which can be interpreted as a linear combination of power-law functions of the type

$$Y(x) = A_0 + \sum_{p=1}^{3} A_p x^{\lambda_p} \tag{1}$$

The fitting function corresponds to the GPD, which we successfully applied in our previous paper [27]. The fitting procedure demonstrates that a set of three power-law functions is sufficient to achieve a fit with a relative error on the order of

1% to 5%. It should also be noted that the values of the power-law exponents $\lambda_p$ can be real or even complex. We will now illustrate the data processing procedure with several figures.

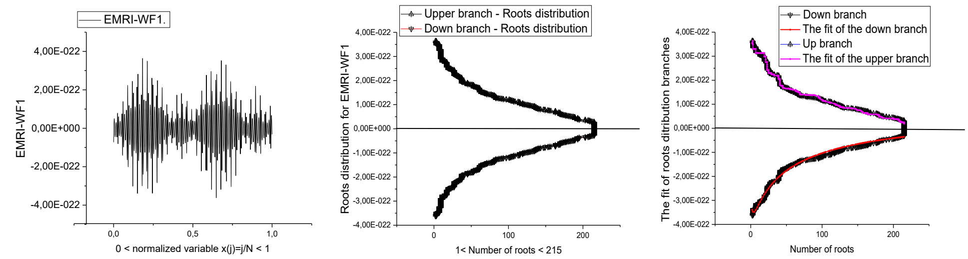


(a) (b) (c)

Fig. 3 – On the left figure (a) EMRI WF-1 is displayed, occupying the interval [–3. 637 · $10^{-22}$, 3.62 · $10^{-22}$] and with parameters shown on the Fig. 1. The central figure (b) is remarkable. It demonstrates the roots distribution of the WF-1 shown on the left figure together with their fit of up/dn branches shown, correspondingly, by solid red lines on the right figure (c).

Applying the eigen-coordinates method [28] to expression (1) one can transform the nonlinear fit into a linear least-squares problem, which allows one to fit the ascending and descending branches of the obtained RD. The fit of the corresponding branches is shown in Fig. 3(c). Thus, we obtain a total of seven fitting parameters for each branch, which can then be used for subsequent analysis. These parameters are shown below in Table 1.

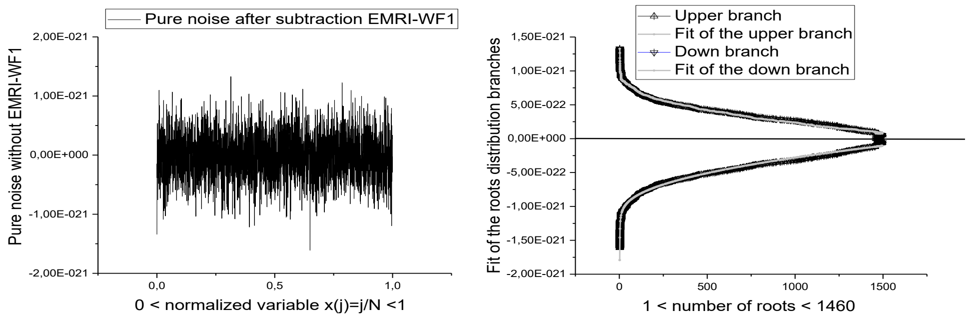


(a) (b)

Fig. 4 – The left panel (a) presents the noise that may obscure WF-1. As can be seen from the right panel (b), the number of roots is changed significantly. If the fitting parameters of the WF are known, the signal can be successfully detected. The fit of the distribution function is shown in panel (b) by gray solid lines. The fitting parameters for the ascending and descending branches of the RD are provided below in Table 1.

*Table 1*

The values of the fitting parameters that characterize the WF-1 roots distribution and its noise shown in Figs. 3 and 4. It is sufficient for the fitting purposes one puts in (1) $A_0 = 0$

| WF-1 | $\lambda_0$ | $\mathrm{Re}(\lambda_1)$ | $\mathrm{Im}(\lambda_1)$ | $\mathrm{Re}(\lambda_2)$ | $A_0$ | $A_1$ | $A_2$ | Rel Err(%) |
|---|---|---|---|---|---|---|---|---|
| Upper branch (signal) | –0.8495 | –0.3925 | 0.0000 | 1.4341 | $-7.693 \cdot 10^{-22}$ | $1.026 \cdot 10^{-21}$ | 0 | 0.13361 |
| Down branch (signal) | –0.6800 | –0.2993 | 0.6206 | –0.2993 | $-5.318 \cdot 10^{-22}$ | $1.996 \cdot 10^{-22}$ | $-4.569 \cdot 10^{-22}$ | 0.22450 |
| Upper Branch (noise) | –0.2972 | –0.1001 | 0.0000 | 0.9012 | $1.549 \cdot 10^{-22}$ | $1.288 \cdot 10^{-21}$ | $-7.933 \cdot 10^{-25}$ | 0.12933 |
| Down Branch (noise) | –2.0088 | –0.0659 | 0.0000 | 0.5872 | $-2.130 \cdot 10^{-21}$ | $-1.34 \cdot 10^{-21}$ | $9.839 \cdot 10^{-24}$ | 0.19504 |

As it is seen in Fig. 1, this presentation is highly convenient and can be used for the complete identification of EMRI WF signal that may be hidden within the noise.

In the same manner, the other WFs hidden within their corresponding noise can be analyzed.

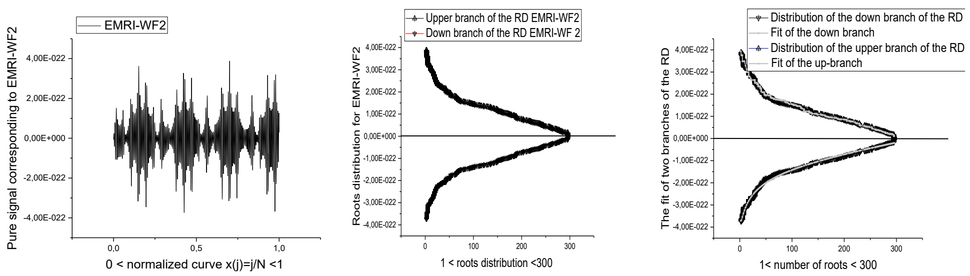


(a) (b) (c)

Fig. 5 – In figure (a) on the left we show the WF-2. As one can see from the central figure (b) the number of roots is slightly changed. These changes can be read in terms of the fitting parameters of the GPD function (1) that are shown below. The right figure (c) shows the corresponding distribution together with their fit shown by grey solid lines. The fitting parameters are listed below in Table 2.

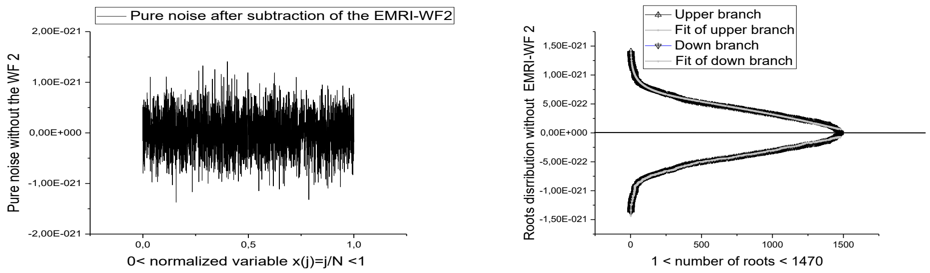


(a) (b)

Fig. 6 – In the left figure (a) we show the noise that covers WF-2. As one can see from the right figure (b) the number of roots is changed. If the fitting parameters of the WF-2 are known then it can be detected. The fit of the distribution function is shown on this figure (b) by grey solid lines. The fitting parameters of the roots for the up/down branches are given below.

*Table 2*

The values of the fitting parameters that characterize the WF-2 roots distribution and its noise shown in Figs. 5 and 6

| WF-2 | $\lambda_0$ | $\mathrm{Re}(\lambda_1)$<br>$\mathrm{Im}(\lambda_1)$ | $\mathrm{Re}(\lambda_2)$ | $A_0$ | $A_1$ | $A_2$ | Rel Err(%) |
|---|---|---|---|---|---|---|---|
| Upper branch (signal) | 1.99275 | –0.2139<br>0.2526 | –0.21391 | 0 | $4.135 \cdot 10^{-22}$ | $2.831 \cdot 10^{-22}$ | 0.1309 |
| Down branch (signal) | 1.10363 | –0.3631<br>0.2437 | –0.36314 | $1.728 \cdot 10^{-22}$ | $-3.415 \cdot 10^{-25}$ | $-8.414 \cdot 10^{-22}$ | 0.1666 |
| Upper Branch (noise) | 2.04709 | –0.20364<br>0.1474 | –0.20364 | $1.011 \cdot 10^{-25}$ | $1.511 \cdot 10^{-22}$ | $1.434 \cdot 10^{-22}$ | 0.1048 |
| Down Branch (noise) | –0.67340 | –0.0912<br>0.0000 | 0.91772 | $-3.252 \cdot 10^{-22}$ | $-1.313 \cdot 10^{-21}$ | $7.467 \cdot 10^{-25}$ | 0.1138 |

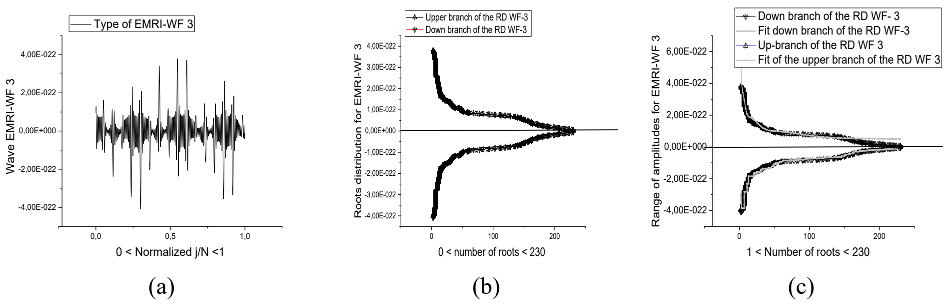


(a) (b) (c)

Fig. 7 – In figure (a) on the left we show the WF-3. As one can see from the central figure (b) the distribution of roots is changed and becomes narrower. These changes can be read in terms of the fitting parameters of the function (1) that are shown below in Table 3. The right figure (c) shows the corresponding distribution together with their fit shown by solid grey lines.

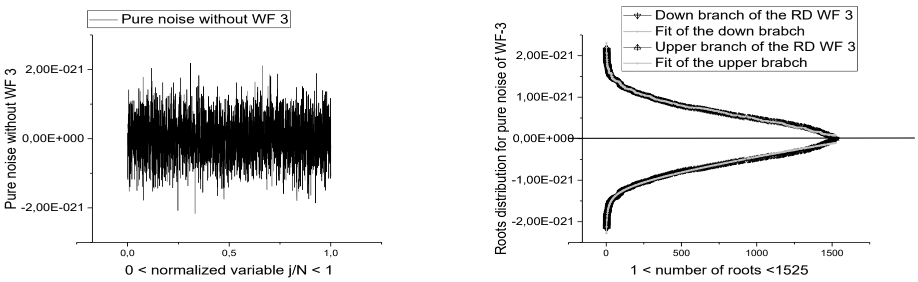


(a) (b)

Fig. 8 – In the left figure (a) we show the noise that can cover WF-3. As one can see from the right figure (b) the number of roots is changed. If the fitting parameters of the WF-3 are known then it can be detected. The fit of the distribution function is shown on this figure (b) by grey solid lines. The fitting parameters of the roots for the up/down branches are given below.

*Table 3*

The values of the fitting parameters that characterize WF-3 roots distribution and the corresponding noise shown in Figs. 7 and 8

| WF-3 | $\lambda_0$ | $\mathrm{Re}(\lambda_1)$ / $\mathrm{Im}(\lambda_1)$ | $\mathrm{Re}(\lambda_2)$ | $A_0$ | $A_1$ | $A_2$ | Rel Err(%) |
|---|---|---|---|---|---|---|---|
| Upper branch (signal) | –0.5105 | –0.5611 / 5.0943 | –0.5611 | $7.551 \cdot 10^{-22}$ | $-6.211 \cdot 10^{-23}$ | $4.657 \cdot 10^{-24}$ | 0.3735 |
| Down branch (signal) | –1.7116 | –0.6756 / 0.0000 | 2.5156 | $1.991 \cdot 10^{-22}$ | $-1.448 \cdot 10^{-21}$ | 0 | 0.2966 |
| Upper Branch (noise) | 1.7428 | –0.1229 / 0.12416 | –0.1229 | 0 | $2.479 \cdot 10^{-21}$ | $3.885 \cdot 10^{-22}$ | 0.0886 |
| Down Branch (noise) | –0.5731 | –0.0906 / 0.0000 | 0.9072 | $-6.036 \cdot 10^{-22}$ | $-1.996 \cdot 10^{-21}$ | $1.212 \cdot 10^{-24}$ | 0.1151 |

### 3.2. ANALYSIS OF RANDOM SEQUENCES WITH TREND

Previous analysis is based on the fitting of corresponding branches of trendless sequences with the help of the GPD. In this section we show how to detect a hidden signal with amplitudes much less than the amplitudes of a trendless sequence that serves a specific container for the hidden signal inside in it. In order to demonstrate the method, we will use the same WF data. We subtract the WF from the noisy signal and prepare "a pure" sequence. We then integrate this sequence relative to its mean value, utilizing the trapezoidal method

$$J_j = J_{j-1} + \frac{1}{2}\left(x_j - x_{j-1}\right) \cdot \left(\Delta y_j + \Delta y_{j-1}\right),$$

$$\Delta y_j = y_j - \text{mean}(y),\ \ \text{mean}(y) = \frac{1}{N}\sum_{j=1}^{N} y_j. \tag{2}$$

and compare two integrated curves with signal and without one with the help of the RDs. Does this roots distribution enable to detect a presence of a weak signal hidden inside the given noise? The SNR of the signal (Fig. 3(a)) relative to the noise (Fig. 4(a)) is defined by

$$\text{SNR} = 10 \cdot \log\left(\frac{\text{Range}(Wf)}{\text{Range}(Ns)}\right) \tag{3}$$

and has the value SNR = –8.16. A comparison of the corresponding integrated noises (with and without the WF) is presented below.

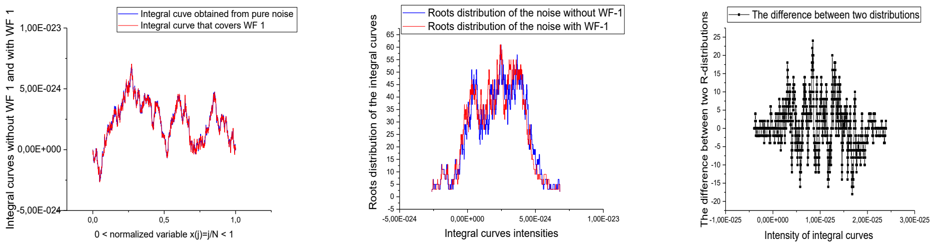


(a) (b) (c)

Fig. 9 – In the left figure (a) we show the integral curves (black – without signal and red – with addition of WF-1) that are used for detection of a weak signal. As one can see from the central figure (b) RDS literally "smudges" a small signal over all amplitudes range and, therefore, it becomes noticeable because of the usage the rotated axes. We stress again that initial OY axis (showing the range of a small signal) becomes OX axis in the RDS and this essential remark becomes important. The last figure (c) determines the difference between number of distribution roots. In the same manner one can consider other given signals. For WF-1 SNR = –6.08.

The same procedure is then repeated for the remaining integrated curves: first for WF-2 (SNR = −7.98 dB), and subsequently for WF-3 (SNR = −7.43 dB).

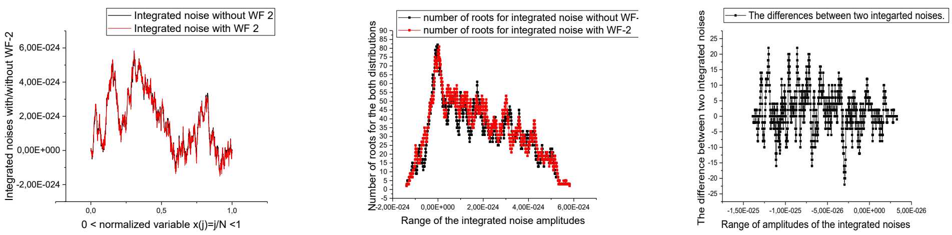


(a) (b) (c)

Fig. 10 – In figure (a) we show the integral curves (black line – without signal and red – with addition of a small WF-2 shown in Fig. 5(a)). These integrated noises are used for detection of a weak signal. In comparison with the previous figure one can notice that integrated curves are different. As one can see from the central figure RDS literally "smudges" a small signal over all range and, therefore, it becomes noticeable because of the usage the rotated axes. The last figure (c) determines the difference between two RD-spectra.

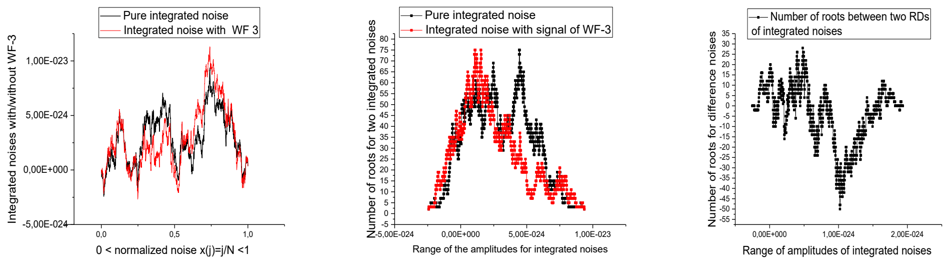


(a) (b) (c)

Fig. 11 – In figure (a) we show the integrated curves (black line – without signal and red – with addition of a small WF-3) that are used for detection of a weak signal. In comparison with the previous figure one can notice that integrated curve is really different. As one can see from the central figure RDS literally "smudges" a small signal over all range of integral curve and, therefore, it becomes noticeable because of the usage the rotated axes. The last figure (c) determines the difference between two RD-spectra.

Finally, the second-type RDS is obtained by calculating the RDs for the differences between the first-order RDs, as illustrated in the right-hand panels of Figs. 9(c) through 11(c). These second-type distributions are presented below in Fig. 12 (a, b, c).

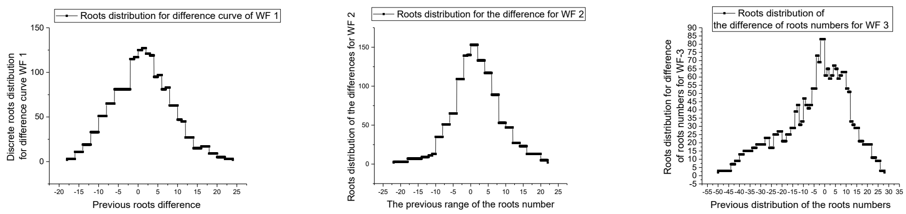


(a) (b) (c)

Fig. 12 – The second type of the RDs calculated for differences of the RD of the first type. From the left figure (a) to the right figure (c) these distributions correspond to integrated noises containing the three WFs, correspondingly.

## 4. RESULTS AND DISCUSSION

In this paper, we propose a novel methodology based on the RDS. Each distribution corresponding to a trendless sequence has two branches, and each branch, in turn, can be expressed using the parameters of the GPD as defined by Eq. (1). Each branch has 6 fitting parameters at least. For simplicity, we set the free fitting parameter $A_0$ to zero, as the resulting relative error does not exceed 1% (refer to the last column in the tables for comparison).

The attractive peculiarities of the proposed RDS are visible within the integral distributions of the trendless sequences. One can receive the RDs for integral curves with signal and without one. The rotation of their distributions by an angle of 90°

(transforming OY to OX) clearly demonstrates a remarkable property. Their roots are smudged over the previous OY axes and because of this property one can obtain the difference between their integral curves containing a hidden signal and without one. These differences are clearly visible in Figs. 9(c) through 11(c). We reiterate that the rotation of the OY axis to the OX axis (OY → OX) causes the number of roots to change, thereby serving as an additional discriminant for detecting weak EMRI GW signals. Figure 12 illustrates the RD of the calculated differences. This additional source of information can serve as a specific fingerprint for comparing the integrated noise with the GWs hidden within it.

REFERENCES


1. P. Amaro-Seoane et al., *The gravitational wave universe with LISA: A cosmo-logical perspective*, Classical and Quantum Gravity **29** (12), 124016 (2012).
2. J.R. Gair, L. Barack, T. Creighton, C. Cutler, S.L. Larson, E.S. Phinney, M. Vallisneri, *Event rate estimates for LISA extreme mass ratio capture sources*, Classical and Quantum Gravity **21**, S1595 (2004).
3. P. Amaro-Seoane et al., *Laser Interferometer Space Antenna*, arXiv:1702.00786 (2022).
4. S. Babak, J. Gair, A. Sesana, E. Barausse, B.S. Sathyaprakash et al., *Science with the space-based interferometer LISA. V: Extreme mass-ratio inspirals*, Physical Review D **95** (10), 103012 (2017).
5. L. Barack et al., *Black holes, gravitational waves and fundamental physics: a roadmap*, Classical and Quantum Gravity **36** (14), 143001 (2019).
6. F.D. Ryan, *Gravitational waves from the inspiral of a compact object into a massive, axisymmetric body with arbitrary multipole moments*, Physical Review D **52**, 5707 (1995).
7. N. Yunes, K. Yagi, and F. Pretorius, *Theoretical physics implications of the binary black-hole mergers GW150914 and GW151226*, Physical Review D **94** (8), 084002 (2016).
8. B.S. Sathyaprakash and B.F. Schutz, *Probing the nature of dark energy with gravitational wave observations*, Living Reviews in Relativity **12** (1), 2 (2009).
9. C. Hopman, *Extreme mass ratio inspiral rates: dependence on the massive black hole mass*, Classical and Quantum Gravity **24** (14), S897 (2007).
10. N.J. Cornish and T.B. Littenberg, *Bayesian inference for gravitational wave astronomy*, Classical and Quantum Gravity **32** (13), 135012 (2015).
11. M. Tinto and S.V. Dhurandhar, *Time-delay interferometry*, Living Reviews in Relativity **17**, 6 (2014).
12. J.R. Gair and K. Glampedakis, *Improved approximation for the gravitational wave flux from extreme mass-ratio inspirals*, Physical Review D **70**, 124015 (2004).
13. F. Feroz, M.P. Hobson, E. Cameron, and A.N. Pettitt, *Importance nested sampling and the MultiNest algorithm*, The Open Journal of Astrophysics **2** (1), 2019.
14. J. Veitch et al., *Parameter estimation for compact binaries with ground-based gravitational-wave observations using the LALInference software library*, Physical Review D **91** (4), 042003 (2015).
15. H. Gabbard, M. Williams, F. Hayes, C. Messenger, and I.S. Heng, *Matching matched filtering with deep networks for gravitational-wave astronomy*, Physical Review Letters **120** (14), 141103 (2018).
16. Alvin J. K. Chua, and Michele Vallisneri, *Learning Bayesian posteriors with neural networks for gravitational-wave inference*, Physical Review Letters **122** (21), 211101 (2019).
17. D. Green et al., *Noise subtraction and parameter estimation in LISA with machine learning*, Monthly Notices of the Royal Astronomical Society **498** (4), 5424 (2020).
18. M. Katz et al., *Advanced noise modeling for LISA*, arXiv:2401.01234 (2024).
19. A. Nousi et al., *Source separation in space-based gravitational wave detectors*, Physical Review D **105** (12), 124056 (2022).

20. A. Romero et al., *Generative models for realistic LISA noise*, Journal of Cosmology and Astroparticle Physics **2020** (8), 9 (2020).
21. L. Barack, *Gravitational self-force in extreme mass-ratio inspirals*, Classical and Quantum Gravity **26** (21), 213001 (2009).
22. S.E. Field et al., *Fast prediction and evaluation of gravitational waveforms using surrogate models*, Physical Review **X 4** (3), 031006 (2014).
23. S. Babak et al., *The Mock LISA Data Challenges: from challenge 3 to challenge*, Classical and Quantum Gravity **26** (9), 094024 (2009).
24. N.J. Cornish, *LISA data analysis using a hybrid swarm-based algorithm*, Classical and Quantum Gravity **25** (10), 105012 (2008).
25. A.J.K. Chua et al., *Efficient and accurate simulation of gravitational-wave signals from extreme mass-ratio inspirals*, Physical Review D **104** (10), 104019 (2021).
26. J.B. Bayle et al., *Global analysis of the LISA data stream with compact binary population models*, Physical Review D **106** (8), 083010 (2022).
27. R.R. Nigmatullin, D. Baleanu, O. Tintareanu, P. Stefanescu, *The Generalized Pareto Distribution: Its Applications to Cosmic Microwave Background*, Romanian Journal of Physics **69**, 403 (2024).
28. R.R. Nigmatullin, *Recognition of nonextensive statistic distribution by the eigen-coordinates method*, Physica A **285**, 547 (2000).